Journal of Alloys and Compounds 509 (2011) 8510–8517

Contents lists available at ScienceDirect

Journal of Alloys and Compounds

journal homepage: www.elsevier.com/locate/jallcom

Effect of speed-ratio on microstructure, and mechanical properties of Mg–3Al–1Zn alloy, in differential speed rolling

W.J. Kim[a,*], B.G. Hwang[a], M.J. Lee[b], Y.B. Park[b]

[a] Department of Materials Science and Engineering, Hongik University, 72-1 Mapo-gu, Sangsu-dong, Seoul 121-791, Republic of Korea
[b] Department of Materials Science and Engineering, Sunchon National University, 315 Maegok, Sunchon, Jeonnam 540-742, Republic of Korea

ARTICLE INFO

Article history:
Received 30 March 2011
Received in revised form 15 May 2011
Accepted 16 May 2011
Available online 23 May 2011

Keywords:
Magnesium alloys
Mechanical properties
Microstructure
Texture
Differential speed rolling

ABSTRACT

The effect of speed ratio (SR) in differential speed rolling on the development of texture and microstructure in Mg–3Al–1Zn alloy was systematically investigated in a wide SR range between 1 and 3 at a fixed thickness reduction of 20%. At low SRs, deformation bands and shear bands were dominant. At high SRs ≥ 2, however, dynamically recrystallized microstructures were developed. The intensity of the basal texture component increased with SR, but decreased to the level of the starting material at high SRs ≥ 2. The occurrence of the dynamic recrystallization at high SRs was attributed to high-dislocation density accumulation and high temperature rise of a deforming sheet due to large plastic deformation of which amount increased with SR. The basal texture weakening at high SRs was attributed to extensive tension twinning that occurred in the basal-oriented matrix, which is rarely observed in conventional rolling. Due to the positive effect of texture and microstructure, tensile ductility improvement was significant as compared to that by symmetric rolling.

1. Introduction

Magnesium alloys have potential as structural materials due to their high specific properties. Grain refinement and texture control in magnesium alloys by thermo-mechanical processing have been widely studied in the recent past to enhance their mechanical properties. Mukai et al. [1] and Kim et al. [2] succeeded in greatly enhancing the room temperature ductility in AZ magnesium alloys by adopting the equal channel angular pressing technique, which rotates the basal poles by ~45° from the pressing direction. In an attempt of improving ductility and strength of Mg alloys by rolling, differential speed rolling (DSR) has been studied [3–7]. In DSR, rotation speeds for upper and lower rolls are different such that extra shear deformation can be induced in addition to through-thickness strain. There are many factors that affect the microstructures and textures of Mg alloys in DSR: roll speed ratio, roll rotational speed, rolling temperature, rolling direction, thickness reduction per pass, etc. Watanabe et al. [5] and Huang et al. [3,4] studied the effect of DSR temperature and thickness reduction per pass on texture and tensile properties at relatively low speed ratios of 1.1–1.2. Kim et al. [6,7], on the other hand, studied the effects of DSR temperature on texture and mechanical properties at a high speed ratio of 3. Despite these works, however, the understanding of the effect of speed ratio on evolution of the microstructure and texture of Mg alloys during DSR is still lacking since the effect of roll speed ratio has never been systematically studied.

In this study, we investigated the effect of roll speed ratio on microstructure and texture of the Mg–3Al–1Zn (AZ31) alloy, covering various speed ratios ranging between 1 and 3. Mechanical properties of the rolled samples were evaluated by tensile testing at room temperature and the obtained results were discussed in terms of correlation with the textures and microstructures.

2. Material and methods

The material used in the current study was Mg–3Al–1Zn (AZ31) alloy processed by strip casting method, 2 mm in thickness, 180 mm in width and 200 mm in length. Rolling was conducted using a rolling mill with a roll diameter of 400 mm. The speed ratio (SR) between the upper and lower rolls varied from 1 to 1.1, 1.2, 1.5, 2 and 3 with the speed of lower roll fixed as 3 rpm. No lubrication was applied during rolling. The sheets were preheated to 513 K and then fed to rollers preheated at 473 K for a thickness reduction of 20% by a single roll pass. For tensile testing, specimens with gauge length of 32 mm were cut from the rolled materials along planes coinciding with the rolling direction (RD). Tensile tests were conducted at room temperature at an initial strain rate of 10^{-3} s^{-1}.

X-ray pole figures were measured using Cu Kα at various thickness layers. To identify an actual thickness layer of the sheet, a parameter $s = \pm 10\Delta x/(d_o/2)$ was introduced, where Δx represents the distance between the respective layer and sample center and $d_o/2$ is the half thickness. The development of textures was analyzed at $s = 9$, $s = 0$, and $s = -9$, respectively. The electron back-scattering diffraction (EBSD) analysis with a scanning step size of 0.3 μm was performed on the longitudinal sections of the rolled sheets possessing the normal direction (ND) and the RD. The EBSD data were processed using the TSL-OIM analysis software. The average grain size was determined with a tolerance angle of 15°.

* Corresponding author. Tel.: +82 2320 1468; fax: +82 2325 6116.
E-mail address: kimwj@wow.hongik.ac.kr (W.J. Kim).

0925-8388/$ – see front matter © 2011 Elsevier B.V. All rights reserved.
doi:10.1016/j.jallcom.2011.05.063

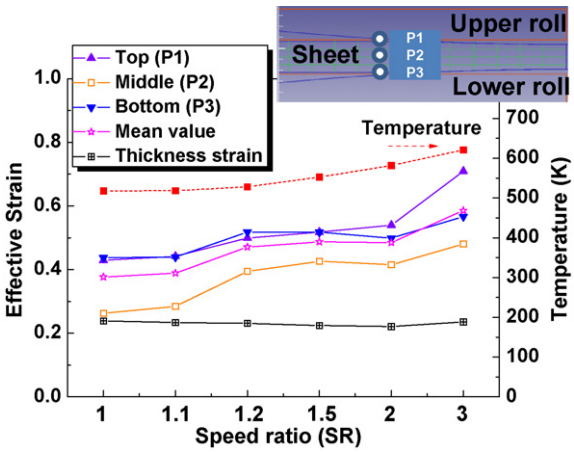

Fig. 1. The FEM simulations in terms of the effective strain, thickness strain, and sample temperature as a function of SR.

The commercial finite-element (FE) code (DEFORM 2D) was employed to analyze the rolling process at different SRs. The friction factor, mechanical and thermal properties of the AZ31 alloy used in the present FE analysis are given elsewhere [8].

3. Results

The total effective strain and thickness strain at different SRs were computed using the FE method and the result is summarized in Fig. 1. There exists a strain gradient along thickness direction, and the strain at the middle layer (p2) is the smallest in each SR. The effective strain in the middle layer at SR of 1 is virtually identical to the thickness strain since no redundant shear strain is generated at the middle layer during symmetric rolling. The effective strains at the top (p1), middle (p2) and bottom (p3) layers continue to increase with SR. The average effective strain calculated based on the local strains measured at the three layers is 0.59 at the highest SR of 3, which is larger by a factor of 1.55 than that accumulated at SR of 1 (0.38). Contribution of shear strain to the total strain can be estimated by extracting the thickness strain (~0.24 at all the SRs) from the average effective strain. According to this result, the contribution of shear strain to total strain is higher at SR of 3 by a factor of 2.5 than that at SR of 1. During rolling, temperature of the sheet increases and this is due to energy conversion from plastic deformation of the sheet and friction at the roll/sheet interface. The sample temperature at the exit tends to increase with SR. For example, the temperature difference at SRs of 1 and 3 is as much as 103 K.

Fig. 2(a)–(c) show the optical microstructures of the as-received and the samples rolled at SRs of 1.5 and 3, respectively. The microstructure of the as-received AZ31 appears overall heterogeneous. It is composed of fine and equiaxed grains that represent the recrystallized microstructure, and coarse and elongated grains that represent the non-fully broken original strip-cast microstructure. Deformation bands and twins are observed inside the coarse grains. Almost homogenous microstructure was achieved at SR of 3. The area fraction of the non-fully fragmented grains (f_{coarse}), which is defined as the grains with dimensions $\geq$ 20 μm, was measured by use of an image analysis software and the result is presented in Fig. 2(d). It is evident that the fraction of coarse grains decreases with SR. The sharp drop in f_{coarse} occurred beyond SR of 1.2, and it measured only 0.05–0.06 at SRs of 2 and 3.

Fig. 3(a)–(f) show the EBSD image quality (IQ) maps observed at the middle of the longitudinal sections of the rolled samples. At SR of 1, deformation bands were developed and mutually crossed, leading to fragmentation of original grains into small domains. Shear bands appear at SR of 1.2 and finely fragmented grains exist along them. At SR of 1.5, the IQ value is quite low, implying that the entire microstructure is full of high density dislocations. Dynamically recrystallized grains with equiaxed shape and well defined boundaries prevail at SRs of 2 and 3. The IQ values are

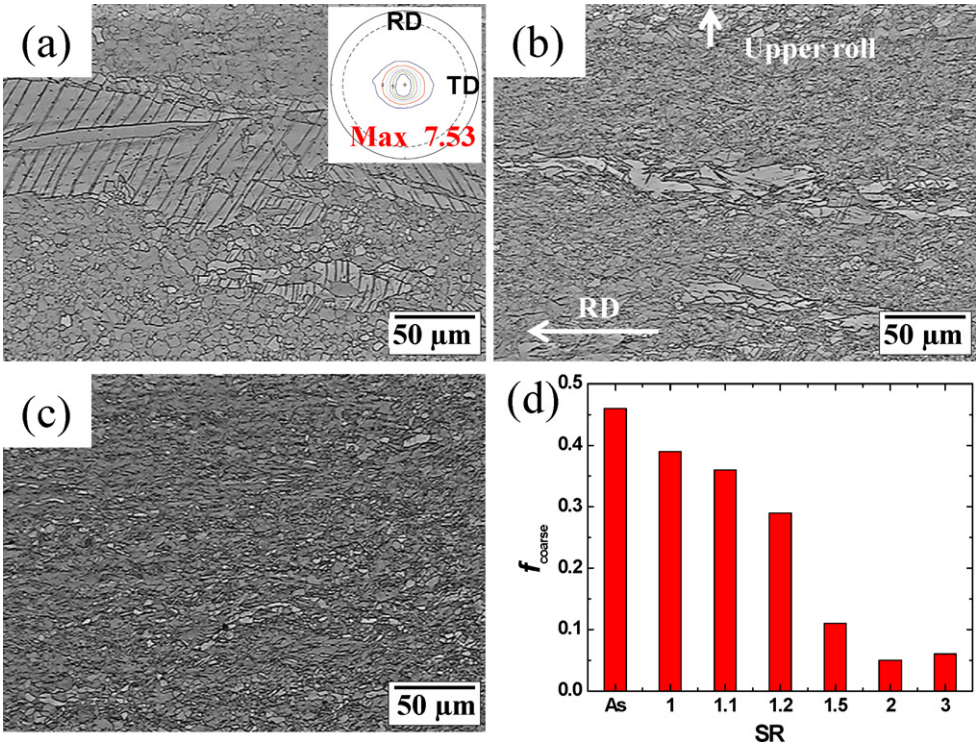

Fig. 2. The optical microstructures of the samples (a) as-received and as-rolled at SRs of (b) 1.5 and (c) 3, respectively. (d) The area fraction of coarse grains as a function of SR. The (0 0 0 2) XRD pole figure measured at $s = 0$ of the as-received sample is presented as the insert.

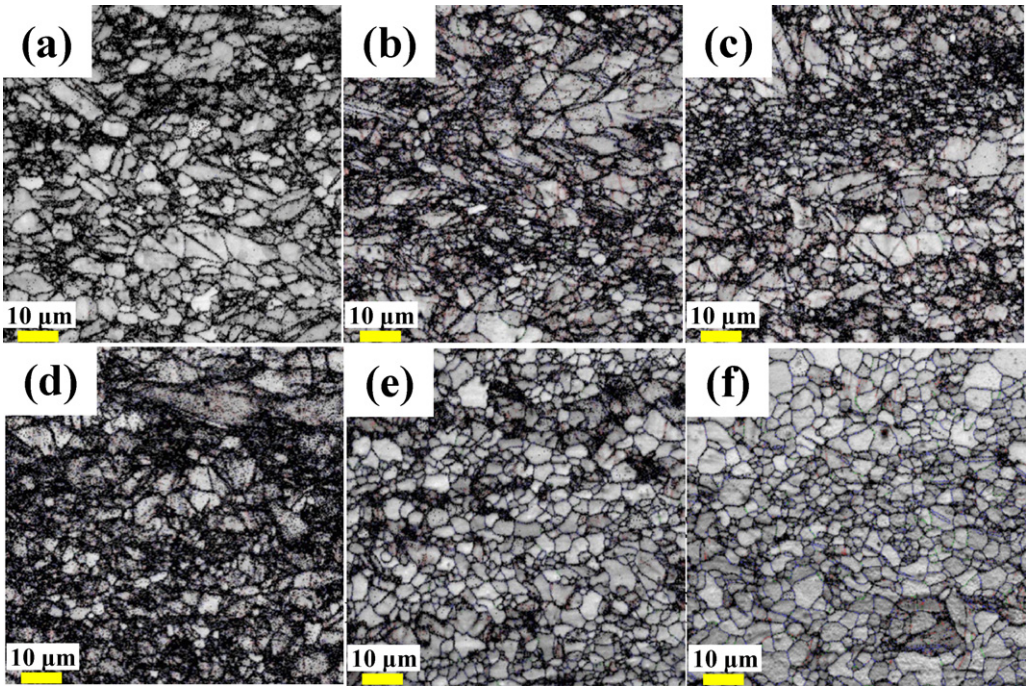

Fig. 3. The EBSD IQ maps observed at $s = 0$ of the RD-ND planes in the samples rolled at SRs of (a) 1, (b) 1.1, (c) 1.2, (d) 1.5, (e) 2 and (f) 3.

accordingly recovered to be high. Fully recrystallized grains fill the whole volume of the specimen at SR of 3, while a small fraction of microstructure remains unrecrystallized at SR of 2.

In Fig. 4, the average grain size, which was determined based on the three grain sizes measured at the top, middle and bottom layers of each material by means of the EBSD analysis, is plotted as a function of SR. It decreases from 9 μm to 5.9 μm after rolling at SR of 3. The fraction of high angle grain boundaries ($\theta > 15^\circ$), on the other hand, decreases from 0.89 to 0.61 and 0.54 after rolling at SRs of 1 and 1.1, respectively, but becomes restored to the level of the starting material at SR of 3 (0.81). Activity of continuous dynamic recrystallization (CDRX), which often occurs in various metals subjected to severe plastic deformation, is known to increase with increasing rate of dislocation storage during deformation and increasing grain-boundary mobility. Higher temperature often provides higher boundary mobility. At the low SRs of 1 and 1.1, CDRX activity would have been limited since the amount of accumulated strain was small and the sample temperature was not so high. For this reason, formation of cells or subgrains with low angle boundaries was resulted. At the high SRs of 2 and 3, the stored dislocation density and the sample temperature were sufficiently high to accelerate CDRX and so formation of recrystallized grains was resulted.

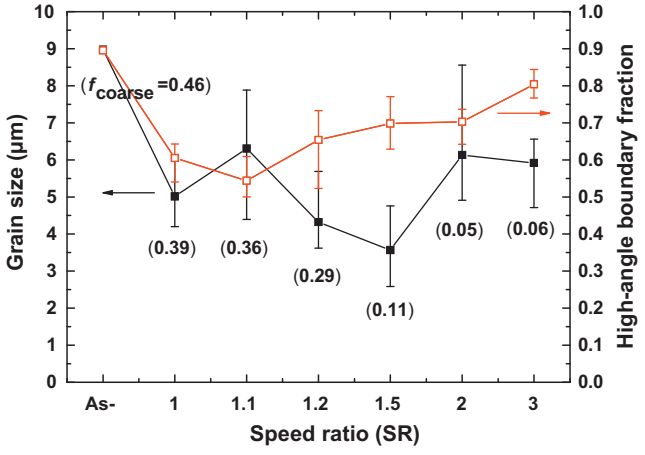

Fig. 4. The average grain sizes and the average fractions of high angle boundaries measured at the top, middle and bottom layers of the samples rolled at different SRs.

Fig. 5 shows the (0 0 0 2) XRD pole figures measured at $s = 0$ $s = -9$ and $s = 9$ in the samples rolled at different SRs. The (0 0 0 2) pole figure measured at $s = 0$ of the as-received sheet is given as an insert in Fig. 2(a). The textures at all the SRs including the initial texture can be approximately characterized by the ND//⟨0 0 0 1⟩ basal fiber texture component, but the intensity distribution and the maximum intensity values are different. At SR of 1, the (0002) poles spread along ± TD. As SR increases, however, the spreading decreases and instead, the poles begin to disperse along ± RD. At SR of 3, a circle-shaped contour of the (0 0 0 2) poles is formed. This variation in the distribution of the basal texture supports that shear deformation promotes the rotation of the basal planes toward the RD [9]. Unlike the previous works in the DSR processed AZ31 alloys [7,10], however, the inclination angles of the maximum basal peak with respect to ND are small at all the SRs even in the surface layers of the sheets where larger shear straining was experienced as compared to the middle layer. This may be resulted since the amount of shear deformation is not so large even at high SRs under the current rolling condition where the applied thickness reduction ratio is small as 20%.

The representative engineering stress–engineering strain curves of the as-received and the samples rolled at different SRs are shown in Fig. 6(a). Three specimens were tested for each material and the average values for yield stress (YS) ultimate tensile stress (UTS), total elongation (ε_t), uniform strain (ε_u) and strain hardening exponent (n) were calculated. The results are presented in Table 1 and the values are plotted in Fig. 6(b). The ε_u was determined based on Considere's criterion and the n value was determined by measuring the slope at the region where the most linear relationship held over the wide range of strain in the $\log \sigma$ vs. $\log \varepsilon$ plot. As SR increases, the YS initially increases, but decreases beyond SR of 1.2. At SR of 2 and 3, the strength is lower

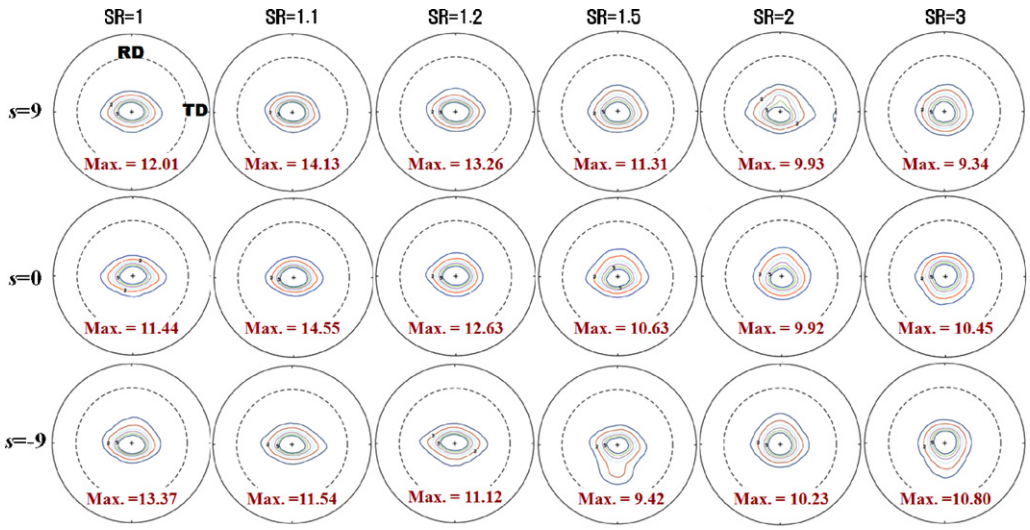

Fig. 5. The (0 0 0 2) XRD pole figures measured at $s = 0$ $s = -9$ and $s = 9$ in the samples rolled at different SRs.

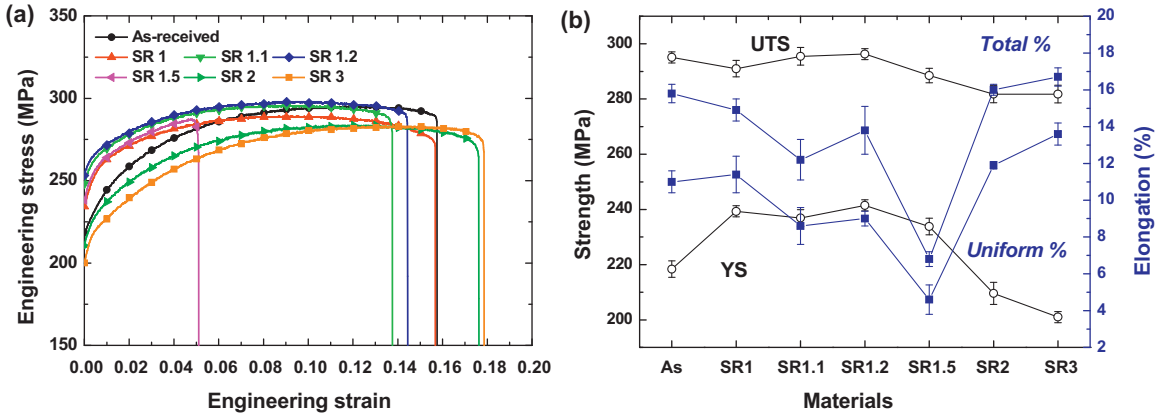

Fig. 6. (a) Engineering stress–engineering strain curves of the samples as-received and rolled at different SRs (b) Strength and elongation measured from these curves as a function of SR.

than that of the as-received. The ε_t and ε_u, on the other hand, tend to decrease as SR increases, but abruptly increase beyond SR of 1.5. The ε_t and ε_u values at SR of 3 (16.7% and 13.6%) are larger compared to those of the received (15.8% and 11%) and those (14.9% and 11.4%) obtained after symmetric rolling (at SR of 1). This ductility improvement at SR of 3 can be attributed to the enhanced strain hardening ability since the n value at SR of 3 (0.16) is larger than the values of the as-received (0.09) and the symmetrically rolled one (0.12). It is worthy of noting that the n value of the AZ31 processed at SR of 3 (0.16) is larger than the n values of the strip-casting processed AZ31 prepared by using symmetric rolling under various thermo-mechanical conditions (0.08–0.14 [11]). This is encouraging since n value is a single most important factor that affects stretch formability of Mg alloys at room temperature [11]. The noticeably small elongation at SR of 1.5 compared to the values at the other SRs may be the result of occurrence of premature failure prior to necking in tension, probably due to development of internal damage such as cracks and voids caused by a high rate of strain hardening during the rolling process.

Table 1
Tensile mechanical properties of the as-received and the samples rolled at different SRs.

Alloy	Condition	YS (MPa)	UTS (MPa)	ε_t (%)	ε_u (%)	n
AZ31	As-received	218.4	295.1	15.8	11	0.12
	SR 1	239.3	291	14.9	11.4	0.09
	SR 1.1	236.9	295.5	12.2	8.6	0.09
	SR 1.2	241.5	296.3	13.8	9	0.09
	SR 1.5	233.8	288.5	6.8	–	0.09
	SR 2	209.6	281.8	16	11.9	0.13
	SR 3	201	281.8	16.7	13.6	0.16

4. Discussion

There are three representative types of twins in pure Mg and Mg alloys: $\{10\bar{1}2\}$ tension, $\{10\bar{1}1\}$ compression and $\{10\bar{1}1\}$ – $\{10\bar{1}2\}$ double twins, which have misorientations of 86°, 56° and 38° around the $\langle 1\bar{2}10\rangle$ axis with the parent grains, respectively. The fractions of these three types of twins were measured by means of EBSD at the top, middle and bottom layers of each material and then the three values were averaged. The calculated values are plotted as a function of SR in Fig. 7. Tension twins are dominant in all the SRs and there is a trend that the fraction of tension twins increases with SR. The values of maximum basal texture intensities measured by XRD at $s = 9$, $s = 0$, and $s = -9$ in the samples rolled at different SRs (shown in Fig. 3) are also presented in the same graph, showing that the texture intensity increases up to SR of 1.1, decreases and then reaches a steady value beyond SR of 1.5.

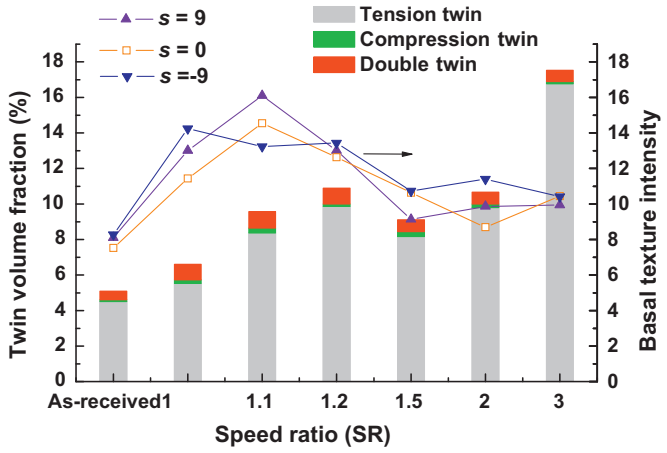

Fig. 7. The average fractions of the components having orientation relationships of three different types of twins, and the maximum intensities of the basal texture component measured by XRD at $s = 9$, 0 and −9.

It is known that conventional hot rolling in magnesium alloys gives rise to the development of the basal texture due to tension twinning [12]. Grains with their *c*-axis are parallel to the compression axis are unfavorably oriented for $\{10\bar{1}2\}$ twinning during hot rolling. On the other hand, grains with their *c*-axis are perpendicular to the compression axis during hot rolling are favorably oriented for $\{10\bar{1}2\}$ twinning. After these grains are deformed by $\{10\bar{1}2\}$ twinning, the basal planes are rearranged by a rotation of 86° <1–210> to be approximately perpendicular to the compression axis [13], leading to strengthening of the basal texture. In contrast, the $\{10\bar{1}1\}$ compression and $\{10\bar{1}1\} - \{10\bar{1}2\}$ double twinning make the basal poles reorient by rotations of 56° $\langle 1\bar{2}10\rangle$ and 38° $\langle 1\bar{2}10\rangle$, respectively, resulting in weakening of the basal texture [14].

Fig. 8(a) and (b) show the typical EBSD images with the corresponding (0 0 0 2) pole figures and the grain shape maps with defined twin boundaries at the SRs of 1.2 and 3, respectively. At SR of 1.2, the fraction of tension twins is much higher (0.17) compared to compression twins (0.001) and double twins (0.005). Also, at SR of 3, the tension twins are dominant over the other twins. The fraction of tension twins is as high as 0.57. At SR of 1.2, most of tension twins are observed along the shear bands of the parent matrix. At SR of 3, on the other hand, tension twins are more ran-

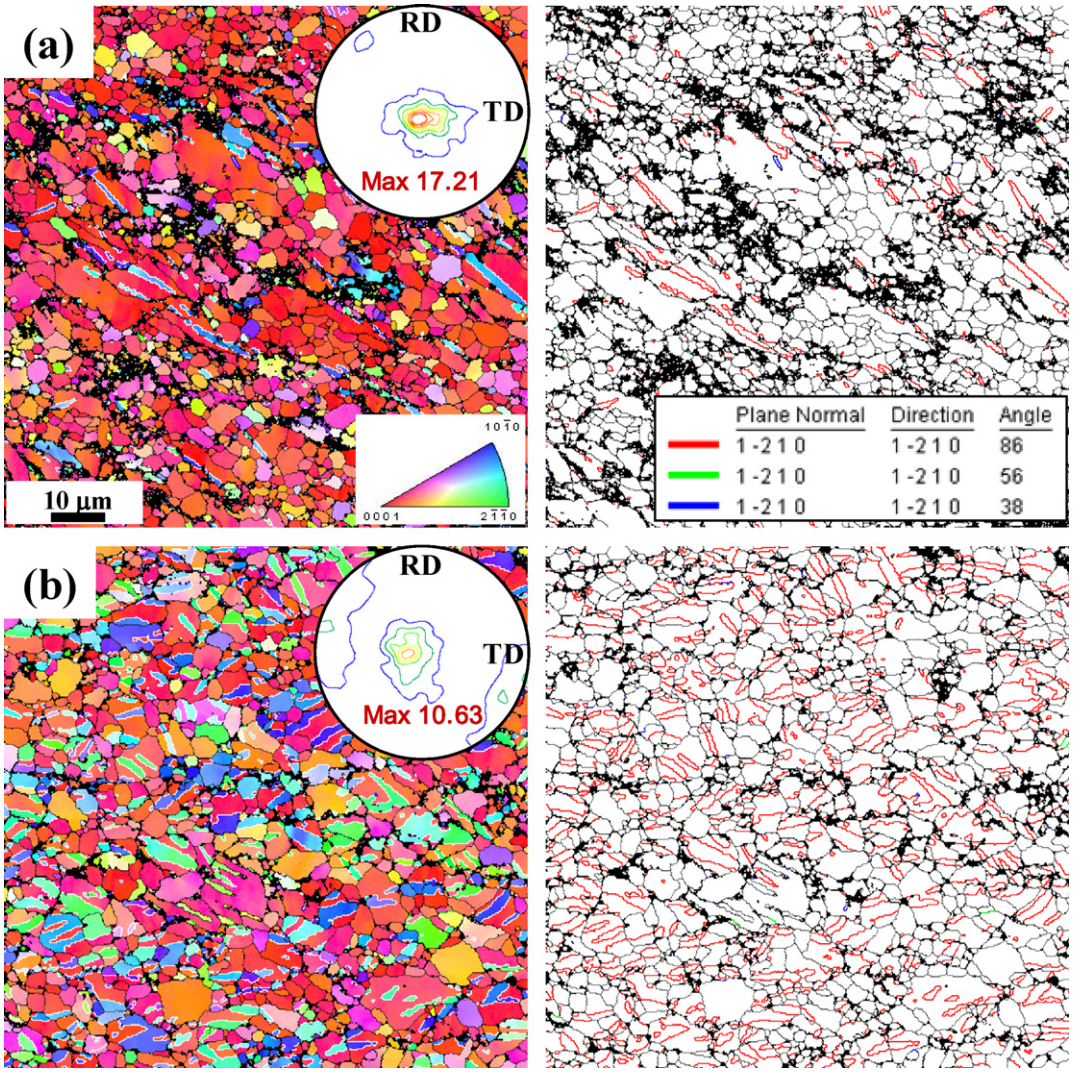

Fig. 8. Typical EBSD images of the microstructures obtained at SRs of (a) 1.2 and (b) 3 with the corresponding (0 0 0 2) pole figures and the grain shape maps with defined twin boundaries.

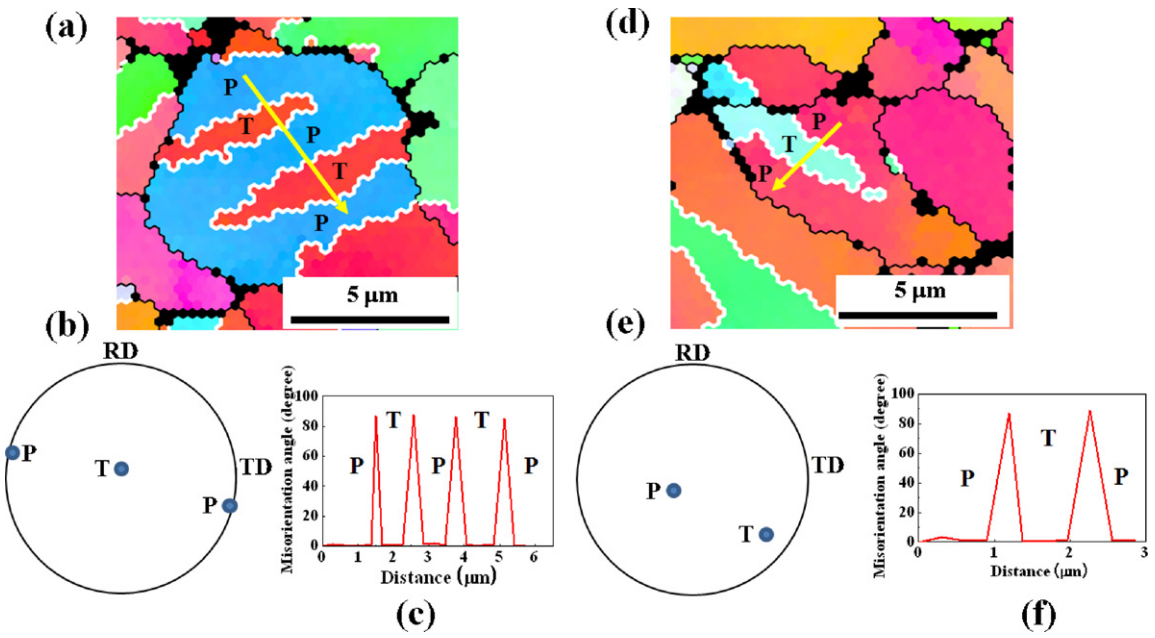

Fig. 9. (a) EBSD map for a grain containing the first type tension twins in the microstructure at SR of 3. (b) ⟨0 0 0 1⟩ orientations of a parent grain and twins and (c) the profile of the misorientation angle along the direction indicated as an arrow in (a). P and T represent a parent grain and a twin, respectively. (d) EBSD map for a grain containing the second type tension twin in the microstructure obtained at SR of 3 (e) ⟨0 0 0 1⟩ orientations of a parent grain and twin and (f) the profile of the misorientation angle along the direction indicated as an arrow in (d).

domly distributed throughout the matrix. Expanding tension twins are frequently encountered, implying that twin growth actively took place during rolling. Grain-like domains having the orientation relationship of tension twin are also observed. When CDRX takes place inside the twins during the continued rolling or when twins nucleated on grains created by CDRX grow to replace the entire grains, the new grains have the similar orientations as the parent twins [15].

The tension twins in Fig. 8(a) and (b) can be classified into two types. The first type is the one that normally observed in conventional rolling. That is, by tension twining in grains with their *c*-axis perpendicular to the compression axis, the basal planes are rotated to be approximately perpendicular to the compression axis. The second type is the one that occurs in the basal-oriented matrix. By twinning, grains with their *c*-axis parallel to the compression axis reorient the basal planes perpendicular to the compression axis. Fig. 9(a) shows a crystallographic orientation map for the first type tension twins found in a grain in the sample rolled at SR of 3, where P and T represent a parent grain and a twinned region, respectively. The twin bands are parallel to each other. As shown in Fig. 9(b), which depicts the ⟨0 0 0 1⟩ orientation of the parent grain and twins, all the twins have an identical crystallographic orientation, indicating that they all were generated from an identical twin variant. The profile of the misorientation angle along the direction indicated as an arrow in Fig. 9(a) is presented in Fig. 9(c), indicating that the misorientation angles at the boundaries are about 85–87°. Fig. 9(d)–(f) show the similar analysis for the second type tension twins found in a grain in the sample rolled at SR of 3. As in the first type tension twin, the misorientation angles at the boundaries between the parent grains and twins are about 86–89°, but the tension twining occurred in the basal-oriented grains.

Fig. 10(a) and (b) show the collection of the first type and the second type tension twins identified in the EBSD image given in Fig. 8(b) and Fig. 10(c) shows the (0 0 0 2) pole figure constructed based on the two types of tension twins. As can be recognized, the second type tension twins are overwhelmingly dominant over the first type twins at SR of 3. The first type twins are a few. Fig. 10(d) shows the collection of the first and the second type tension twins identified in the EBSD image given in Fig. 8(a) and the (0 0 0 2) pole figure constructed based on the the EBSD data. At SR of 1.2 also, the second type tension twins are dominant over the first type tension twins, which are few. At lower SRs of 1 and 1.1, even the second type tension twins are rare. This observation indicates that the fraction of the second type tension twins increases with SR, while the first type tension twins remain few at all the SRs. Tension twins in the basal-oriented matrix is known to comprise three different variants [15], but as shown in the (0 0 0 2) pole figures for the second type tension twins at SRs of 1.2 and 3 (Fig. 10(c) and (e)), one specific variant is dominantly activated. This is different from the previous report [14] that all the three variants were operated in compression of Mg [14]. This specific variant selection may be made since redundant shear stress is induced in the specific direction during DSR.

Formation of the second type tension twins under compression appears to be difficult since compression twinning, rather than tension twinning, easily occurs when the *c*-axes in the basal-oriented grains are being compressed. There have been, however, reports that during unloading of a highly compressed specimen, the *c*-axis of the parent grains could experience tensile stresses generated along the loading direction [14,16]. For this hypothesis to be valid, tensile stress along the loading direction that develops during unloading should be higher at higher SRs. Further study needs to verify this point.

In order to examine the influence of twinning on the final HRDSR texture, the whole texture in Fig. 8(b) was decomposed into several texture components comprising the parent grains ($0 < \Delta\theta < 20^\circ$) and the twins and/or grains with the crystallographic relationships of double twins ($33^\circ < \Delta\theta < 43^\circ$), compression twins ($51^\circ < \Delta\theta < 61^\circ$) and tension twins ($81^\circ < \Delta\theta < 91^\circ$). This is shown in Fig. 11. The result shows that twinning, especially tension twinning, plays an important role in weakening the overall texture by counteracting the strong basal texture of the parent grains.

It is known that non-basal slips such as prismatic slip and rotational dynamic recrystallization (RDRX) weaken the basal texture [17]. The enhancement of these activities may also contribute to the texture weakening at the high SRs. This is possible because as tem-

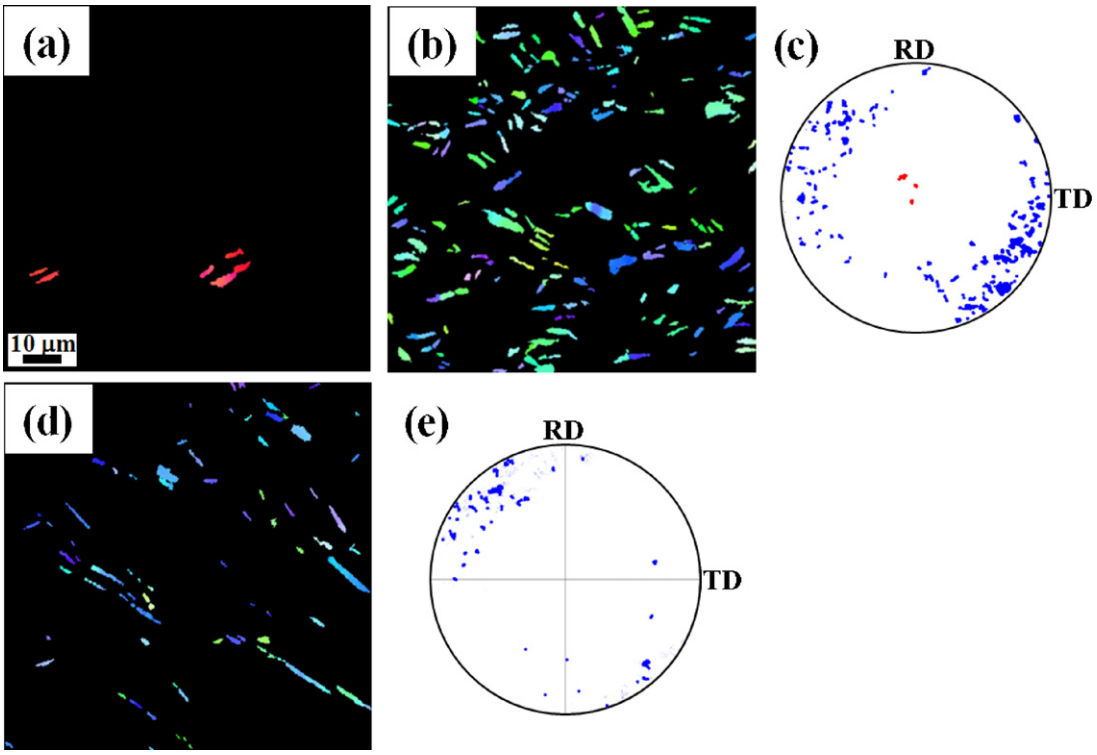

Fig. 10. (a) The first type of and (b) the second type of tension twins identified in the EBSD image given in Fig. 8(b) and (c) the corresponding (0 0 0 2) pole figure. (d) The first and the second type of tension twins identified in the EBSD image in Fig. 8(a) and (e) the corresponding (0 0 0 2) pole figure. The (0002) poles corresponding to the first type tension twins are represented by red color, while the second type twins are represented by blue color. (For interpretation of the references to color in this figure legend, the reader is referred to the web version of the article.)

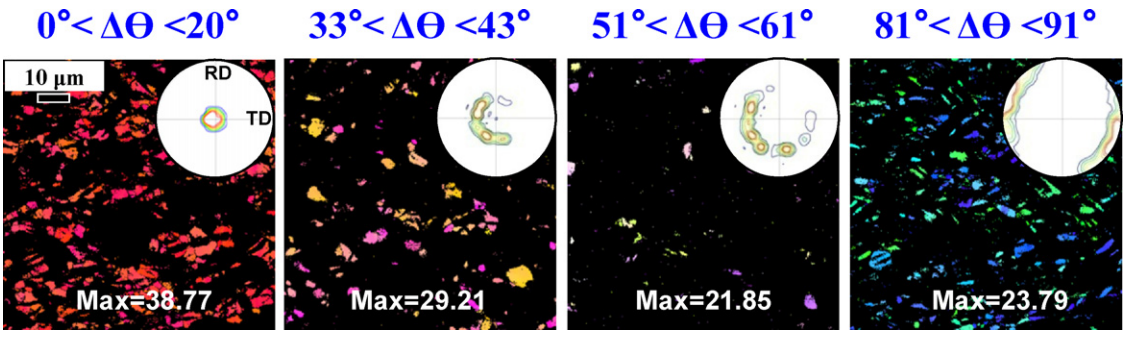

Fig. 11. Microtexture components of a part of the EBSD map shown in Fig. 8(b) are separately presented in terms of the misorientation angle, $\Delta\theta$, which defines the angular distance between the ND and the ⟨0 0 0 1⟩ direction at each point measured by EBSD.

perature of a deforming body increases with SR, the difference in critical resolved shear stress (CRSS) between the basal slip and the non-basal slips decreases and grain-boundary mobility for RDRX increases. Remind that the temperature difference at SRs of 1 and 3 is estimated to be about 100 K.

The mechanical properties of Mg alloys can be affected by grain size, dislocation density and texture. As the grain fragmentation, the dislocation density and the basal texture intensity increase, the strength of materials would increase. As SR increases initially, the strength increases since the basal texture intensity, the dislocation density and the grain fragmentation increase. At SR of 2 and 3, however, the strength sharply decreases. This is resulted from the reduction of dislocation densities by occurrence of CDRX and the reduction of the maximum basal texture intensities by tension twinning in the basal-oriented matrix. The strength at SRs of 2 and 3 is lower than that of the as-received despite having higher maximum basal texture intensity and finer grain size. This may be attributed to the presence of a large fraction of coarse and elongated grains (46%) in the as-received, which possess high-dislocation density in deformation bands and twin boundaries formed within them (Fig. 2(a)). Tensile ductility behavior as a function of SR can be also explained in terms of grain size, texture and dislocation density. At low SRs, tensile elongations are relatively small due to the highly increased dislocation density inside the matrix during rolling, which limits the strain hardening during tensile deformation. Strengthening of the basal texture should also exert a negative effect on ductility. At high SRs, on the other hand, the ductility improves since the basal texture intensity and the dislocation density are low, and the grain size is small.

5. Summary

In this study, we systemically examined the effect of roll speed ratio on the microstructure, texture and mechanical properties of

Mg–3Al–1Zn (AZ31) alloy in a wide range of roll speed ratio. The obtained results are follows;

(1) According to the FE simulation results, the effective strain accumulated during rolling increased with SR and this was due to increase of amount of shear deformation. The temperature of sheet was predicted to increase during rolling due to the heat generated by intensive plastic deformation and high friction. The temperature rise increased with SR.
(2) Unlike at low SRs including symmetric rolling, recrystallized microstructures with relatively low intensities of basal texture were obtained at high SRs ≥ 2, resulting in improvement of total and uniform elongations. At SR of 3, recrystallized grains filled the whole volume of the specimen since the stored dislocation density and the sample temperature were sufficiently high to trigger extensive CDRX.
(3) The relatively low intensities of basal texture at high SRs ≥ 2 compared to low SRs were resulted from extensive tension twinning that arose in the basal-texture matrix. Activity of this type tension twinning increased with SR, which played an important role in weakening the basal texture intensity by counteracting the strong deformation texture of the parent grains at high SRs.
(4) Differential speed rolling at high SRs is potentially useful in improving the room temperature formability of the strip-casting processed Mg alloys that has limit in amount of thermo-mechanical working due to constraint of a limited thickness dimension.

Acknowledgments

This study was supported by a grant from the Fundamental R&D Program for Core Technology of Materials funded by the Ministry of Knowledge Economy, 2009. One of the authors (Y. B. Park) acknowledges the financial assistance from the World Preimium Material project through the Korean Ministry of Knowledge and Economy.

References

[1] T. Mukai, M. Yamanoi, H. Watanabe, K. Higashi, Scr. Mater. (2001) 89.
[2] W.J. Kim, C.W. An, Y.S. Kim, S.I. Hong, Scr. Mater. 47 (2002) 39.
[3] X. Huang, K. Suzuki, A. Watazu, I. Shigematsu, N. Saito, Scr. Mater. 60 (2009) 964.
[4] X. Huang, K. Suzuki, N. Saito, Scr. Mater. 60 (2009) 651.
[5] H. Watanabe, T. Mukai, K. Ishikawa, J. Mater. Process. Technol. 182 (2007) 644.
[6] W.J. Kim, J.B. Lee, W.Y. Kim, H.T. Jeong, H.G. Jeong, Scr. Mater. 56 (2007) 309.
[7] W.J. Kim, M.J. Lee, B.H. Lee, Y.B. Park, Mater. Lett. 64 (2010) 647.
[8] Y.H. Ji, J.J. Park, W.J. Kim, Mater. Sci. Eng. A 454–455 (2007) 570.
[9] P. Yang, L. Wang, X. Li, L. Meng, Acta Metall. Sinica (Engl. Lett.) 23 (2010) 63.
[10] X. Huang, K. Suzuki, A. Watazu, I. Shigematsu, N. Saito, J. Alloys Compd. 479 (2009) 726.
[11] D.H. Kang, D.W. Kim, S. Kim, G.T. Bae, N.J. Kim, Scr. Mater. 61 (2009) 768.
[12] E.A. Calnan, C.J.B. Clews, Philos. Mag. 42 (1951) 919.
[13] S.E. Ion, F.J. Humphreys, S.H. White, Acta Metall. 30 (1982) 1909.
[14] L. Jiang, J.J. Jonas, R.K. Mishra, A.A. Luo, A.K. Sachdev, S. Godet, Acta Mater. 55 (2007) 3899.
[15] T. Al-Samman, G. Gottstein, Mater. Sci. Eng. A 490 (2008) 411.
[16] M.D. Nave, M.R. Barnett, Scr. Mater. 51 (2004) 881.
[17] M.T. Perez-Prado, J.A. del Valle, J.M. Contreras, O.A. Ruano, Scr. Mater. 50 (2004) 661.